Title

Three-dimensional graphene foam based triboelectric nanogenerators for energy systems and autonomous sensors

Authors

Emma Keel,[1] Ammara Ejaz,[1] Michael Mckinlay,[1] Manuel Pelayo Garcia,[1] Marco Caffio,[2] Des Gibson,[1,3] Carlos García Nuñez[1,*]

[1]*Institute of Thin Films, Sensors and Imaging, University of the West of Scotland, SUPA, Paisley PA1 2BE, Scotland, UK*
[2]*Integrated Graphene Ltd., Stirling FK8 2DJ, Scotland, UK*
[3]*Albasense Ltd, Paisley PA1 2BE, Scotland, UK*

** Corresponding author at: Institute of Thin Films, Sensors and Imaging, University of the West of Scotland, Paisley PA1 2BE, Scotland, UK*
e-mail address: carlos.garcianunez@uws.ac.uk

Abstract

In this work we investigate the potential of three-dimensional graphene (3DG) foam as an active layer in triboelectric nanogenerators (TENGs) and as an energy harvesting power source for autonomous sensors. A series of comprehensive measurements have been carried out to test the output characteristics of 3DG-TENG under cyclic mechanical stimulus, capable of operating TENG in contact-separation mode at different frequencies, gap distances between electrodes, and applied pressures. The triboelectric response of 3DG-TENG (with an effective surface of 16 cm^2) showed maximum open-circuit voltage (V_{oc}) and short-circuit current (I_{sc}) of 400 V and 105.7 μA respectively when stimulated at 3 Hz (*contact-separation frequency*) and 70 mm (*optimum gap distance*). Under the same conditions, a maximum output power (P_{out}) of around 10.37 W/m^2 using an external load resistance of 40 MΩ; this is an order of magnitude lower resistance than that needed with other graphene based TENG variants. 3DG-TENG exhibited great stability in the output characteristics with 15,000 cyclic mechanical stimuli and a retention percentage in P_{out} above 95%. This is a significant improvement with respect to other carbon based TENG`s, which show enhanced deterioration of TENG performance due to material transfer between electrodes and plastic deformation of triboelectric materials. Simulations of TENG V_{oc} using distance dependent model determined high triboelectric charge densities in the range of mC/m^2. Here, we also demonstrate the potential of 3DG-TENG as an energy supply for energy storage devices, and also an active layer in an autonomous pressure sensing platform for anonymous room occupancy monitoring in smart buildings.

Keywords: 3D graphene; triboelectric nanogenerator; energy harvesting; self-powered sensors

1. Introduction

The great advances achieved in 5G communication, and the successful miniaturisation of sensors and electronics have boosted the rapid development of the so-called Internet of Things (IoT)[1]. IoT devices and the new concepts of Internet of Everything (IoE) and Internet of Nano Things (IoNT) devices are planned to be utilised in a large range of sectors, including point-of-care health monitoring, mobile devices, navigation, automobiles, smart buildings, and manufacturing industry (Figure 1) [2]. In 2020, the number of IoT devices interlinked worldwide reached around 10 billion, with a forecast for 2030 to have more than 100 billion IoT devices [3]. The high cost of electricity and incremental energy demand from IoT devices require new green energy sources, high efficiency energy harvesting & storing systems and low-power consumption (or batteryless self-powered/ autonomous) sensors [4,5]. This strategy will prevent the constant replacement of batteries in trillions of devices [6], and will reduce the utilisation of wires, making the IoT technology of the near future to be wireless and energy autonomous.

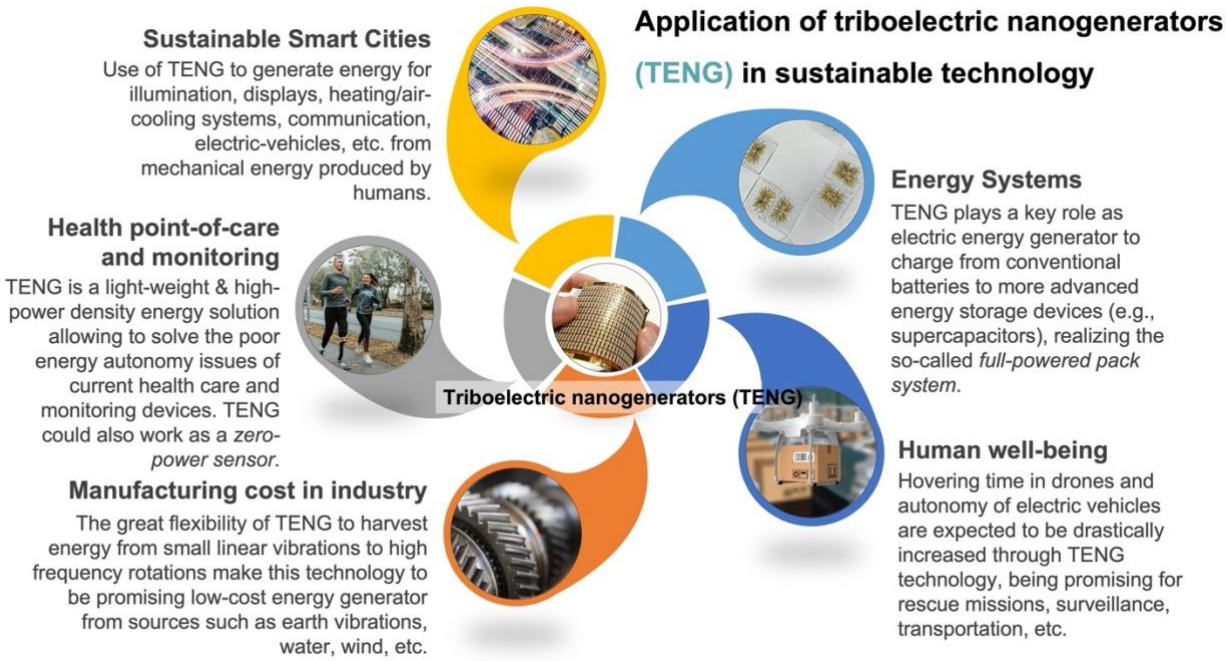

Figure 1. Diagram of TENG utilisation in various applications requiring electric energy.

Mechanical energy is one of the most abundant and versatile energy sources available in nature. In the case of humans, one could easily understand that our daily actions could produce energy from milliwatts to a few watts. For that to happen, we need to find a high efficiency technology capable of transforming mechanical energy – currently wasted in the environment – into useful electrical energy essential to power not only small IoT electronic devices and sensors but also more power-hungry apparatus, e.g., electric cars, and drones (Figure 1). Triboelectric nanogenerators (TENGs) have been proposed as promising technology to harvest mechanical energy from low frequency vibrations (0.1 to 10 Hz) such as those mentioned above. Since the first publications on TENGs in early 2012 [7], their characteristics and fundamentals have been thoroughly studied [8]. Those investigations included TENGs for self-powered sensing platforms [9], theoretical working principle of TENGs [10], giant energy harvesting from ocean waves (so-called *blue energy*) [11], role of TENGs on IoT devices [12], and power management of TENGs [13]. Despite the number of publications, and advantages offered by TENG devices, the technology is still the subject of intensive investigation, aiming to address drawbacks of this promising energy harvesting technology. These include high internal impedance (from MΩ to GΩ depending on the material and structure), low durability, limited short-circuit current (nA to μA), structural changes (material deterioration and degradation over time), and post-stress conditions [14].

TENG consists of two electrically dissimilar materials that create electric power when they are brought into contact and subsequently separated [7][10]. These energy harvesters comprise of a low fabrication cost, are light-weight, miniaturised and easy to integrate, the latter as a consequence of the great adaptability of the device design [8,15–17]. However, TENGs have exhibited high output impedance due to the inherent capacitive structure, leading to a low-energy supply efficiency when the TENG is directly connected to an external load, either to power general electronics or charging energy storage devices with low impedance [13]. TENG presents a great mechanical-to-electrical energy conversion rates above 85% and record power densities above 500 W/m^2 [12], showing the highest open-circuit voltage (V_{oc}) compared to its counterparts. As such TENGs are promising for transformation into a high current to power small to large electronic devices and sensors [18]. In addition to development of new power management modules (PMMs) [13], TENG performance has been tuned through different strategies, including: i) triboelectric material selection [19], ii) TENG design [12,16,17], and iii) TENG working mode [10,20]. Material selection follows the so-called triboelectric series, where materials are classified based on their electron affinity. Essentially, the selection of an electropositive material (also known as tribopositive material) and an electronegative material (tribonegative material) is expected to exhibit enhanced triboelectric effect. Of course, this assumption is subjected to the design of the TENG, thus, further improvement of the TENG output power has been demonstrated

by operating TENG in different modes [10,20], and dry/wet treatment of triboelectric materials to achieve nanostructured morphologies.

Low dimensional carbon materials such as carbon nanotubes (CNT) and graphene possess a unique combination of mechanical flexibility, high electron mobility and chemical stability, making them promising candidates for energy applications and for those reasons they have been explored as electropositive materials in TENG [21]. Moreover, these materials present good conductivity, light weight, and easy synthesis procedure, as well as wide variety of carbon structures, including 1D CNT [22], 2D single layer graphene (SLG), 3D graphene foam (3DG), shear exfoliated graphene (SEG) [23], laser induced graphene (LIG) [24], uncrumpled graphene (UG) [25], and crumpled graphene (CG) [25][26]. Table 1 presents a review of the carbon based TENG, exhibiting record values of V_{oc}, short circuit current (I_{sc}) and output power density (P_{out}), as well as, their operation frequency and best load resistance (R_{load}), the latter, useful for the application of TENG on wearable and portable IoT devices. Carbon based TENG has demonstrated great potential over conventional materials, e.g., SEG-PDMS TENG exhibiting powers 40 times higher than same TENG devices but based on Al-PDMS triboelectric layers [23]. CG as a derivative of graphene, presents high work-function controllability and rough surface, which is beneficial for improving the output power of TENG, and hence, was also successfully used as a triboelectric layer, exhibiting a remarkable enhancement of TENG output characteristics when applying a mechanical strain on graphene. CG obtained pre-stretching graphene 300% of its initial size, exhibited 83 V, 25.78 μA and 2,500 mW/m^2. This effect was associated to a reduction of the work function upon the application of mechanical strain, as well as, the enhancement of the effective contact area and surface roughness of pre-stretched graphene [25]. It is worth noting, that CG-TENG presents one of the lowest internal impedances among all the graphene based TENG, as demonstrates the lowest R_{load} around 2 MΩ showing the maximum output power (*see* Table 1). The utilisation of CG has demonstrated a drastic increase of the P_{out} from 130 mW/m^2 obtained in the case of UG produced by chemical vapor deposition (CVD) [25] up to 2,500 mW/m^2 (CG-PDMS) [25]. Moreover, the pairing of the tribopositive material with a dissimilar tribonegative material, must be selected carefully in order to enhance TENG performance. For example, TENG based on CG and graphite as triboelectric materials have shown low P_{out} of 15 mW/m^2 [26], which is a factor 170 lower than those obtained in TENG using CG-PDMS. It is worth noting, the greatest increase of the P_{out} in graphene based TENG, has been observed in LIG [24] with P_{out} of 2,361 mW/m^2 and 3,056 mW/m^2 when pairing with polyimide and polyurethane triboelectric electrodes, respectively. These results of P_{out} are closer to the record values obtained in CNT base TENG, with P_{out} 8,000 mW/m^2 mainly produced due to the random networks formed in CNTs structures, reducing the loss of triboelectric charges [22]. Those random networks could be observed even in large density in graphene foams, like the one presented in this work, making graphene foam to have a great potential as a triboelectric material with ultra-low energy loss.

Table 1. Comparison of TENG based on different carbon materials as a triboelectric layer, and their output characteristics, including open circuit voltage (V_{oc}), short circuit current (I_{sc}) and output power (P_{out}), obtained at an operation frequency, and load resistance (R_{load}). Table arranged from highest to lowest P_{out}.

Triboelectric materials		**TENG output characteristics**					
Electropositive	**Electronegative**	**Open circuit voltage, V_{oc} (V)**	**Short circuit current, I_{sc} (μA)**	**Output power density, P_{out} (mW/m^2)**	**R_{load} (MΩ)**	**Operation frequency (Hz)**	**REF**
3DG foam	PET	400	105.7	10,372	40	3	This work
CNT	PDMS	383	25	8,000	30	2	[22]
LIG	Polyurethane	1750	40	3,056	-	-	[24]
CG	PDMS	83	25.78	2,500	2	2	[25]
LIG	PI	3500	60	2,361	70	-	[24]
SEG	PDMS	233	0.731	131.4	200	1.5	[23]
CVD UG	PDMS	18.7	6.6	130.0	2	2	[25]
CG	Graphite	15	-	15	-	-	[26]

CNT: Carbon nanotube; **LIG**: laser induced graphene; **CG**: Crumpled Graphene; **3DG**: 3D graphene; **SEG**: shear exfoliated graphene; **PI**: Polyimide; **PET**: Polyethylene terephthalate; **CVD UG:** Chemical vapor deposited uncrumpled graphene.

Before, we study the results obtained in 3DG TENG, from Table 1 it is obvious from all the graphene structures, 3DG TENG in this work presents the highest power density of 10.37 W/m^2 with a moderately low R_{load} of 40 MΩ,

surpassing the record values obtained by CNTs based TENG. 3DG is a variant of graphene with a high surface area and porosity, both expected to be highly beneficial for the successful formation of a triboelectric interface and the reduction of charge losses. The key to 3DG formation is the use of contact electrodes made of materials with different electron affinities. In solid state physics, the electron affinity is a surface property of a material which does not alter due to e.g., doping, but is affected by the crystallinity, chemistry, and texture of the surface. In this regard, 3DG presents a unique surface chemistry among all the graphene morphologies, and as such is expected to show a unique electron affinity in the study of TENG. Graphene electron affinity, as a carbon-based material is expected to be positive. Studies carried out on single layer graphene probe electron affinities of around 2.6-4.5 eV for this material [27]. In this scenario, the most effective strategy to design a TENG based on graphene would be to select second electrodes made of a material exhibiting a negative electron affinity. There are many materials showing negative electron affinities, including Kapton, PET, PVC and PDMS materials, typically chosen due to their compatibility with flexible substrate manufacturing processes.

In this work, we have designed, fabricated, and characterised TENG devices working in contact-separation mode, based on 3DG and polyethylene terephthalate (PET) as tribopositive and tribonegative materials respectively. 3DG-TENG output characteristics have been studied, including V_{oc}, I_{sc} and P_{out} as a function of device operation parameters, i.e., contact-separation frequency, maximum electrode distance, contact pressure and external R_{load}. Moreover, 3DG-TENG electric outputs have been tested over long periods of time to evaluate the robustness, feasibility, and stability of the devices as energy source. This work demonstrates that 3DG possesses a unique porous structure enhancing the contact surface during the mechanical compression of the TENG subjected to external vibrations. This novel property compared to its carbon counterparts leads 3DG to accumulate higher surface charge densities, hence exhibiting higher output powers than other graphene based TENG. The electric properties of 3DG were also evaluated, showing lower internal impedance, making 3DG-TENG to be more integrable with external circuits than conventional TENG. That was successfully demonstrated by using TENG as energy source to power energy storage devices, also probing its validity as self-powered sensor in an energy autonomous sensing platform.

2. Materials and Methods

2.1 Fabrication of TENG based on 3DG

The 3DG material used in this work is a 3DGii™ material grown by a proprietary process patented by Integrated Graphene Ltd [28], consisting of a catalyst free method to grow graphene with a foam morphology directly onto a 125-μm thick Kapton polymide flexible substrate (Kapton® HN from UK insulations Ltd) to prevent the damage caused by its transfer to foreign substrates (Figure 2(a)). The deposition process is carried out using a hard mask to limit the area of the 3DG deposited on the substrate (Figure 2(a1)). This method allows low-cost growth of 3DG at A4 paper size. In this work, we have restricted the study of TENG devices using a 3DG with areas of $5\times15mm^2$ and $40\times40mm^2$ (i.e., $75mm^2$ and 1,600 mm^2).

The characteristics of the 3DG used in this work, including the morphology (pore size and density) and structure (defects density and number of carbon layers) were analysed by scanning electron microscopy (SEM) at 20 kV (S4100 cold FEG from Hitachi), grazing-incidence X-ray diffraction (GIXRD) analysis (D5000 from Siemens) Cu Kα radiation at 40 kV/30 mA, and Raman spectroscopy (DXR3 Raman imaging microscope from ThermoFisher) using a laser wavelength of 532 nm, and reported elsewhere [29]. Briefly, the resulting 3DG exhibited a high level of uniformity as represented in the 3D schematic diagram of Figure 2(a1) and further supported by the photograph of Figure 2(a2). The high density of pores with micrometric size observed by SEM in this 3DG (Figure 2(a3)), makes this material to be light-weight, and unique for the generation, transfer, and storage of charge.

In this work, we have further analysed the surface characteristics of 3DG through the study of surface wettability and roughness. The analysis of the surface wettability was carried out using an optical contact angle meter (CAM200 from KSV Instruments Ltd, **Error! Reference source not found.**(a) in the Supplementary Material). The results presented in **Error! Reference source not found.**(b), indicate that the 3DG is hydrophobic, with a high contact angle of 138.52^o found in 5 different areas under analysis. This result implies a poor adhesiveness, poor wettability, and low solid surface free energy of 3DG. For the sake of completion, the roughness of the 3DG material has been also characterised using stylus profilometry (Dektak3ST stylus profiler, from Veeco). The measurements were carried

out at low scan speed of 20 μm/s and using a light force of 1 mN. The results presented in Figure S2 (Supplementary Material) probe a rough surface with a roughness estimated around 2.4±0.5 μm.

For the sake of completion, the porosity of the material has been also analysed in this work, expanding our initial studies reported elsewhere [29]. From our SEM studies (*see* **Error! Reference source not found.** and **Error! Reference source not found.**), we can conclude that the 3DGii™ material consists of porous structure with different geometries and sizes. From **Error! Reference source not found.**(a), one could understand that porous comprises from rectangular to circular shapes. **Error! Reference source not found.**(b) shows the analysis carried out in ImageJ to identify the number porous using the colour contrast of the image. For that analysis, a threshold mask was applied (*see* **Error! Reference source not found.**(c)), allowing to determine the mean pore size and the effective surface area of 3DG. The area under analysis was 1,125 μm^2, resulting in a number of pores of around 30, i.e, 0.027 pores per μm^2. This study also concludes that 3DGii™ material consists of both open and closed cell, the latter as pointed out by the green arrows in **Error! Reference source not found.** (b). **Error! Reference source not found.**(c) is a representative example of rectangular shape pore with a long and short axis of 7.11 and 4.07 μm, resulting in a pore area of 28.94 μm^2. ImageJ was also used to inspect different areas of the same SEM image (*see* **Error! Reference source not found.**(a1-3)) resulting in similar values of roughness than those obtained by profilometry (Figure S2). Moreover, this image analysis software, was used to simulate the 3D plot of the 3DG material as presented in **Error! Reference source not found.**(b).

After 3DG deposition onto the flexible substrate, one edge of the 3DG was metallised using inkjet printing method (Figure 2(b)). An Ag conductive path was printed on 3DG as illustrated by the 3D schematics of Figure 2(b1) and (b2). To prevent any damage of the metallised areas, a protective layer was deposited on top Ag as schematically presented in Figure 2(c1,c2) and in the photograph of Figure 2(c3). That concludes the fabrication of the tribo-positive electrode based on 3DG. The tribo-negative electrode consisted of an ITO 130-nm thick film (conductivity 45-65 Ω/□) deposited on a PET 5-mm thick substrate (No.639303 from Merck). Figure 2(d) shows a 3D schematic diagram of the two electrodes during the separation stage (*see* figure legend for more details about materials and structure).

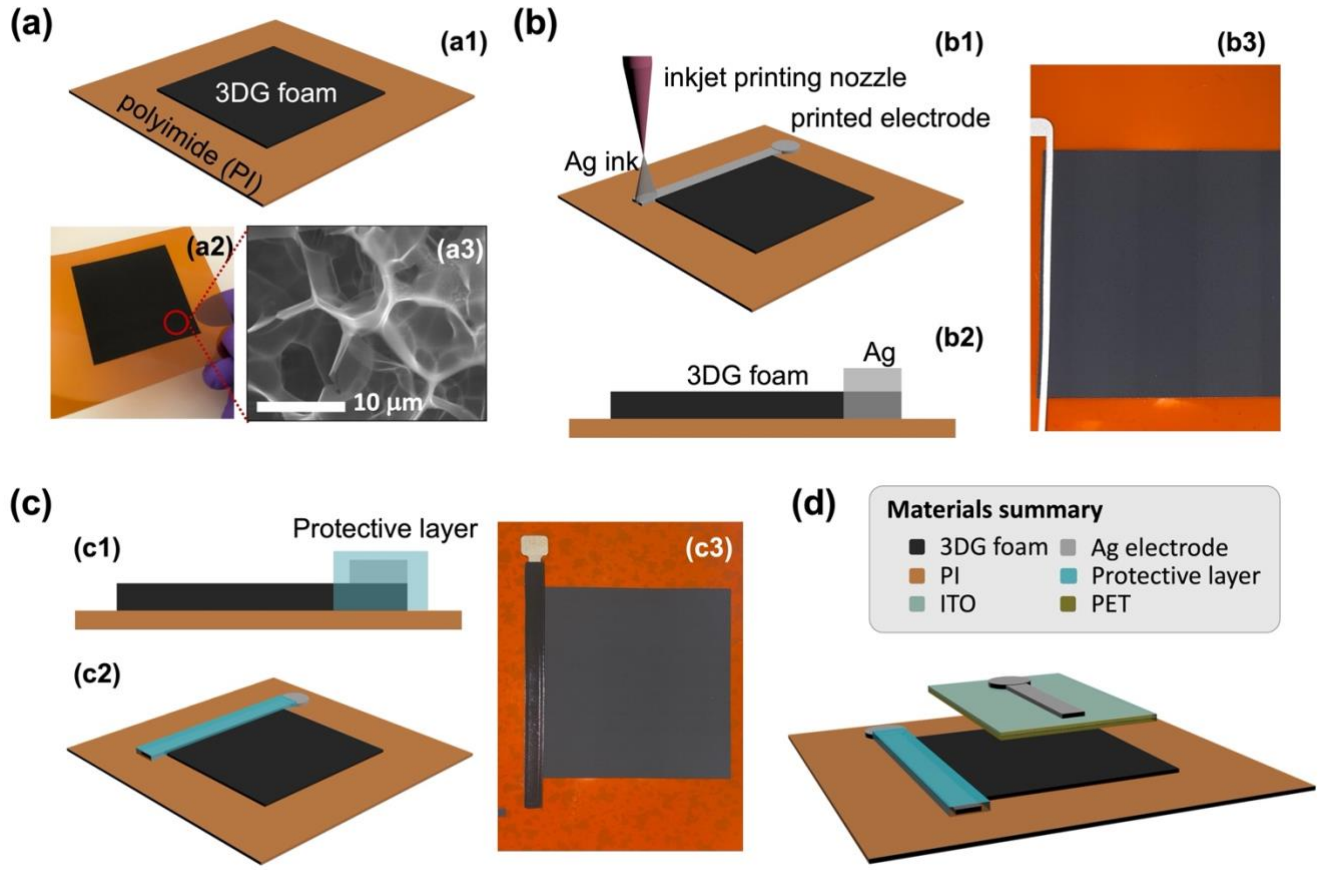

Figure 2. (a) Deposition of 3DG on a flexible substrate; (a1) 3D CAD schematic diagram showing the resulting 3DG deposited on PI substrate; (a2) Photograph of the 3DG patterned directly on PI substrate; (a3) SEM image presenting the porous structure of 3DG. (b) Ag electrodes inkjet printed on 3DG; (b1) perspective and (b2) side views of the layer structure; (b3) photograph of the Ag electrodes printed on 3DG. (c) 3D schematic diagram of the 3DG electrode, right after the encapsulation of the conductive Ag paths; (c1) side and (c2) perspective views of the layer structured after electrode encapsulation and (c3) photograph of the resulting 3DG tribopositive electrode. (d) Diagram presenting the TENG materials, including 3DG electrode (*bottom*) and PET electrode (*top*).

The experimental method described in Figure 2, was utilised to carry out the individual preparation of tribo-positive and tribo-negative electrodes compatible with the characterisation setup that will be described later. In this work, we have also explored a simple and effective design to integrate both 3DG and PET electrodes in a portable TENG, making the resulting device to be more compatible with portable applications. For that, 3DG based TENGs have been designed with a standard vertical configuration, where two electrodes were vertically stacked, using two spongy separators, allowing their contact during the pressure stage, and separation during the release stage. Further details about the fabrication steps of these single cell based 3DG-TENGs are described in **Error! Reference source not found.** (Supplementary Material).

2.2 Characterisation of TENG

2.2.1 TENG working principle

The portable TENG devices presented in **Error! Reference source not found.** were characterised by tapping them at various frequencies (1-4 Hz), and pressures. These tapping experiments were carried out directly by hand on the portable device and by attaching the portable TENG to a laboratory-based setup Figure 3 designed to increase the reproducibility of the results (*see* insets of Figure 3, also Video 1 in Supplementary Material). To understand better the energy generated by these devices, Figure 3 summarises the working principle of TENG devices presented in this work. The figure contains also a small legend detailing the materials used for the electrodes and triboelectric materials. At the centre of the figure, one could find a characteristic V_{oc} peak measured as a function of time. The peak formed during the contact-separation experiments could be described in 4 stages. In the stage (1), the so-called

pressed stage both triboelectric materials are in mechanical contact, resulting in the creation of a triboelectric layer. That effect is also known as charge electrification, and essentially consists of the separation of positive and negative charges at both sides of the interface.

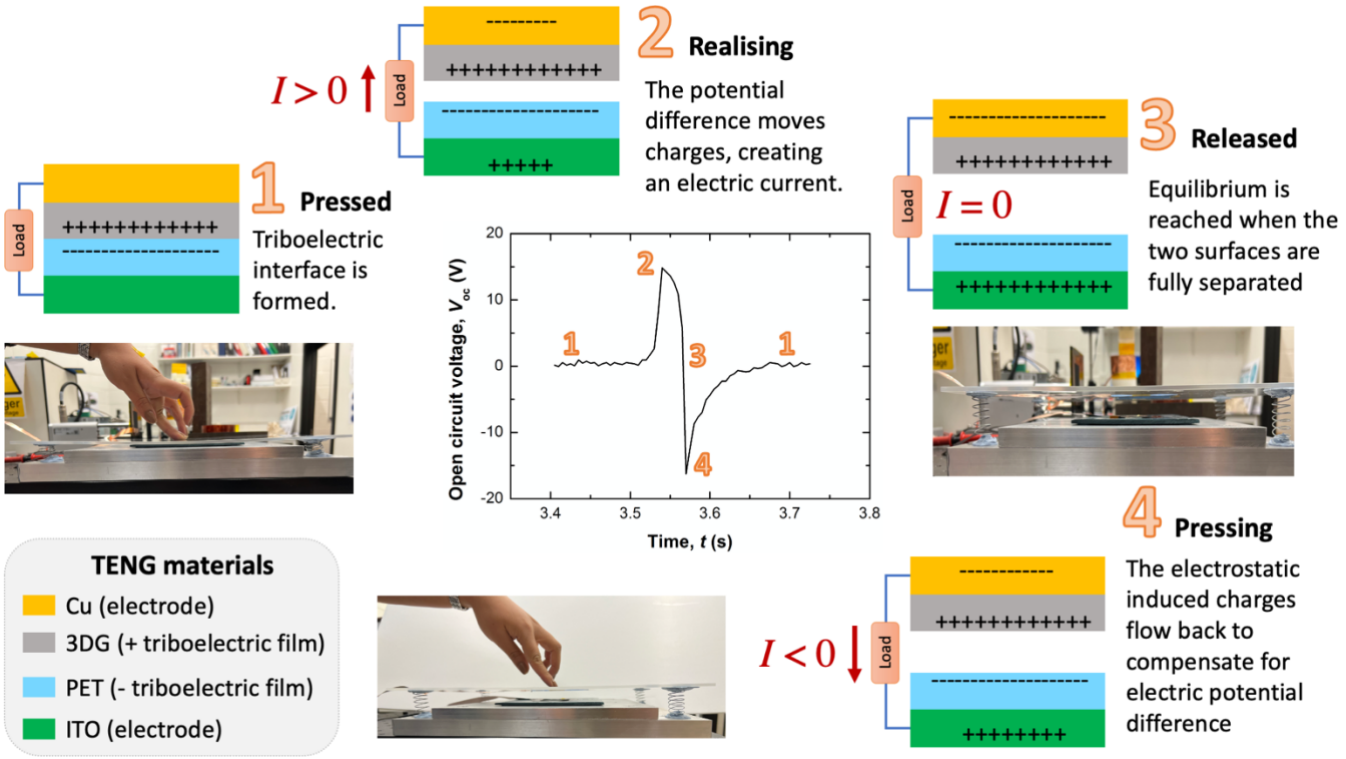

Figure 3. Schematic diagram of TENG working principle. The centre of the figure shows a characteristic V_{oc} peak observed during contact-separation experiments, describing the stages of the energy generation: (1) pressed; (2) realising; (3) released; (4) pressing. Photographs show the laboratory-based system to characterise manually the output characteristics of TENG (*see* also Video 1 in the Supplementary Material).

Here, the electron affinity of the materials plays a key role. 3DG acts as electropositive material transferring negative charges to PET (electronegative material). The contact and separation of these two materials requires a number of cycles in order to reach a constant charge density, also known as triboelectric charge density (σ_T). As such it has been observed that TENG exhibits an increase of the V_{oc} over time due to the dynamic change of σ_T related to the hysteretic behaviour of the contact force response in these devices [30]. Once the TENG reaches the stationary state (i.e., V_{oc} saturates), the energy generation could be used to produce a constant electric power. For that reason, it is a common practice to 'warm up' TENG devices for a short period of time prior to their use as energy source, ensuring the generation of a constant output power. In the stage (2), when both materials are being released (or separated due to the effect of an external force) a small gap is formed between the two materials, and an electric field is generated by the two opposite charges as the distance is separated between them.

In order to screen that potential difference between the two electrodes (V), electrons will be driven to flow from one electrode to the other through the external load. Once the electric potential is fully screened, i.e., $V = 0$, the current in the external circuit is zero (*see* stage 3 in Figure 3). From the released position, if the electrodes are pressed one towards the other (stage 4), the triboelectric charges, that did not exist in the original stage, and in particular the induced potential difference still existing as one could see in the schematic diagram, will begin to decrease to zero, producing a transfer of charge flowing back to their origin through the external load. As it happens in the case of stage (2), when stage (4) is initiated, the current is maximum (min voltage), and when the materials become in close proximity, the voltage will be maximum because both the screening effect in the electrodes is minimum and the distance between electrodes is minimum.

2.2.2 Automatic actuation-experimental arrangement

To understand the energy generation of the TENG, both electrodes have been attached to an automatic actuation system capable of electrode contacting and separation at a controlled frequency, gap distance, and pressure. This system enables long term cyclic test (i.e., thousands of contact-separation cycles) to estimate the percent of retention of the TENG. Figure 4 shows a schematic diagram of the setup, comprising both metrology and actuation parts. In the actuation part (*see* right panel in Figure 4), one of the electrodes was attached to a vertical platform mounted on a X-Y stage fixed to an optical table. The second electrode was attached to a dynamic plate mounted on a linear motor with a stroke of 100 mm and a maximum force of 67.1 N (DM01-23x80F-HP-R-100_MS13 from Quinn systems). In the Supplementary Material, Video 2 illustrates the standard operation of the TENG tester for a specific speed, acceleration, and gap distance between electrodes.

For the frequency study, the linear motor was programmed to travel a fixed distance (gap between electrodes), increasing the speed and the acceleration to cover a wide range of frequencies (*see* **Error! Reference source not found.**, Supplementary Material). To measure the pressure exerted by the dynamic plate to the static one, a compression-based load cell (No. 414-0859, from RS components) was attached to the rear part of the static platform. The pressure of the dynamic stage exerted on the static stage during the contact step was measured in the equivalent conditions utilised during the TENG characterisation (i.e., speed, acceleration, deceleration, and gap). Further information about the load cell calibration as a function of the contact pressure (**Error! Reference source not found.**), gap distance (**Error! Reference source not found.**) and contact-separation frequencies (**Error! Reference source not found.**) parameters could be found in the Supplementary Material.

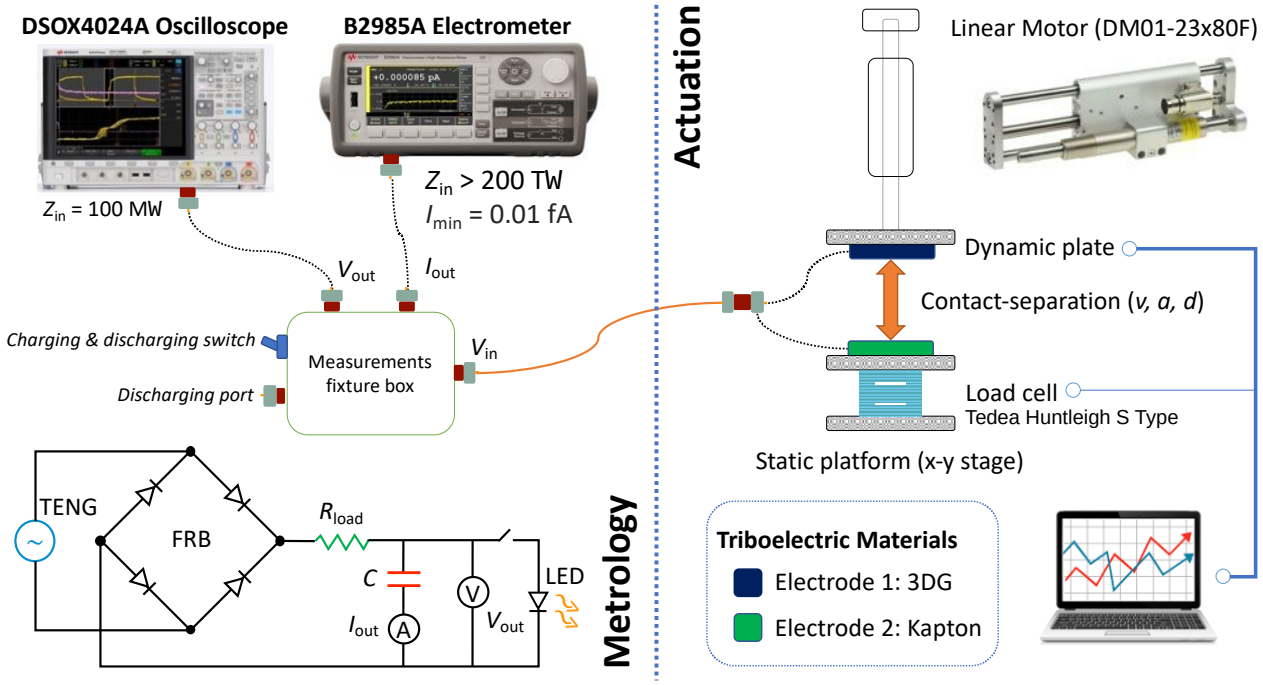

Figure 4. Schematic diagram of the automatic actuation setup built to characterise TENG devices. Left panel (*Metrology*) describes the metrology of the setup, including voltage and current measurements, as well as a fixture box to characterise electric properties of capacitors and loads. Right panel (*Actuation*) presents the linear motor, stages and load cell utilised to control the contact-separation frequency, gap and pressure utilised during the experiments.

For the electric characterisation (*see* left panel in Figure 4), the wires from the two triboelectric materials were soldered to a BNC cable, and the cable connected to a fixture box capable of functioning either in voltage or current modes. In voltage mode, the output of the box was connected to an oscilloscope (DSOX4024A Oscilloscope from Keysight) through a 100 MΩ input impedance probe (BKPR2000B-ND from B&K Precision), ensuring the accurate measurement of the V_{oc} (*see* Video 3 in the Supplementary Material). In the current mode, the box allows the exchange of a R_{load} to characterise the I_{sc} as a function of R_{load}. The output of the box was connected to an electrometer with an input impedance above 200 TΩ and a resolution of 0.01fA (B2985A Electrometer from Keysight). Both

oscilloscope and electrometer were connected to the PC via USB and interfaced through NI Labview, allowing the measurement of output voltage V_{out} and output current (I_{out}) as a function of time and for various contact-separation frequencies, gap distances and pressures. TENG output characteristics consist of AC peaks (Figure 3). The cyclic spectra obtained in the studies were analysed using a Python script, carrying out the identification of the peaks (maxima and minima), the calculation of the mean (for the maxima and minima) and their standard error, and finally the estimation of the peak-to-peak voltage, used here as V_{out}.

The fixture box showed in Figure 4 also has a charging/discharging switch, an energy storing device input inside the box (to prevent noise effects) and a discharging output port (mainly used to drive small devices such as LEDs, displays, actuators, etc.). In the voltage mode, the Labview interface allows monitoring the energy storing device charging (e.g., capacitor, supercapacitor, or battery) and associated discharging cycle with connected load. In current mode, and with the high precision provided by the electrometer, the fixture box enables monitoring of both current and charge densities flowing to the capacitor together with the potential leakage current with time. To correct the noise observed in some of the capacitors charging curves, we have applied the so-called Savitsky-Golay smoothing method, utilising 15 points of window, without boundary conditions, and applying a polynomial order of 2.

All the characterisation described above has been carried out enclosing the TENG setup inside a PVC box, with insulating bands attached to its basement, preventing any effect of the surrounding environment on the TENG characteristics. A smart thermo-hygrometer (H5075, from Govee) has been installed inside the box to monitor via Bluetooth the relative humidity and the temperature during the measurements of the TENG. Results presented in the next section correspond to relative humidity and temperatures ranged between 30-32% and 15-17 ºC, respectively.

2.3 Theoretical analysis of TENG output characteristics

Distance dependent model (DDM) has been used here to simulate V_{oc} and I_{sc} of 3DG-TENG as a function of gap distance between electrodes. Fitting of the experimental results with simulations identified the characteristic triboelectric charge density (σ_T), as a key parameter to optimise the performance of TENG. From DDM [20], the expression for V_{oc} is as follows:

$$V_{oc}(\sigma_T, \varepsilon_{3DG}, \varepsilon_{PET}, z, w) = \phi_1 - \phi_2 \quad (1)$$

where ϕ_1 and ϕ_2 are the electric potentials of triboelectric materials (Figure 3). These potentials depend on both material properties and device structure. The former includes σ_T and the dielectric permittivity of the tribo-positive (ε_{3DG}) and tribo-negative (ε_{PET}) materials. The latter comprises the gap distance (z), and the width (w) of the square triboelectric materials (in this work, w_{3DG} and w_{PET} are the same). For the sake of clarity, the expression for the electric potential is given by Equation 2:

$$\phi_i = \frac{\pm\sigma_T}{\pi\varepsilon_i}[M(x)]_{x_i}^{x_i+z} \quad (2)$$

where $M(x)$ is a periodic function that depends on the relative position of the electrodes with respect to the maximum gap distance; x_i includes x_{3DG} and x_{PET} and represents the thickness of the triboelectric materials. The V_{oc} expression (Eq. 1) was calculated across a range of z, and then, using the non-linear curve fit, the unknown σ_T value was obtained statistically. Simulations have been done with a x_{3DG} of 4 μm, x_{PET} of 25.3 μm, a w of 40 mm, a z ranged between 10 and 90 mm, ε_{PET} of $3.3\varepsilon_0$, and ε_{3DG} ranged between $2\varepsilon_0$ and $8\varepsilon_0$ (ε_0 being the dielectric permittivity of vacuum).

3. Results and Discussion

3.1 Miniaturised TENG

Firstly, we present the characteristics of the miniaturised TENG with an effective area of 5×15mm^2 (i.e., 75 mm^2), limited by the 3DG exposed area (Figure 5(a)). In this section, electric characterisation of this small TENG is described, including V_{oc} characterised as a function of the contact-separation pressure (Figure 5(b)), and frequency (Figure 5(c,d)), as well as the voltage, current and output power measured as a function of the R_{load} (Figure 5(e,f)). The section will conclude with a demonstration of power generation from mechanical energy and transfer of charge to an energy storage device with different capacitances (Figure 5(g,h)).

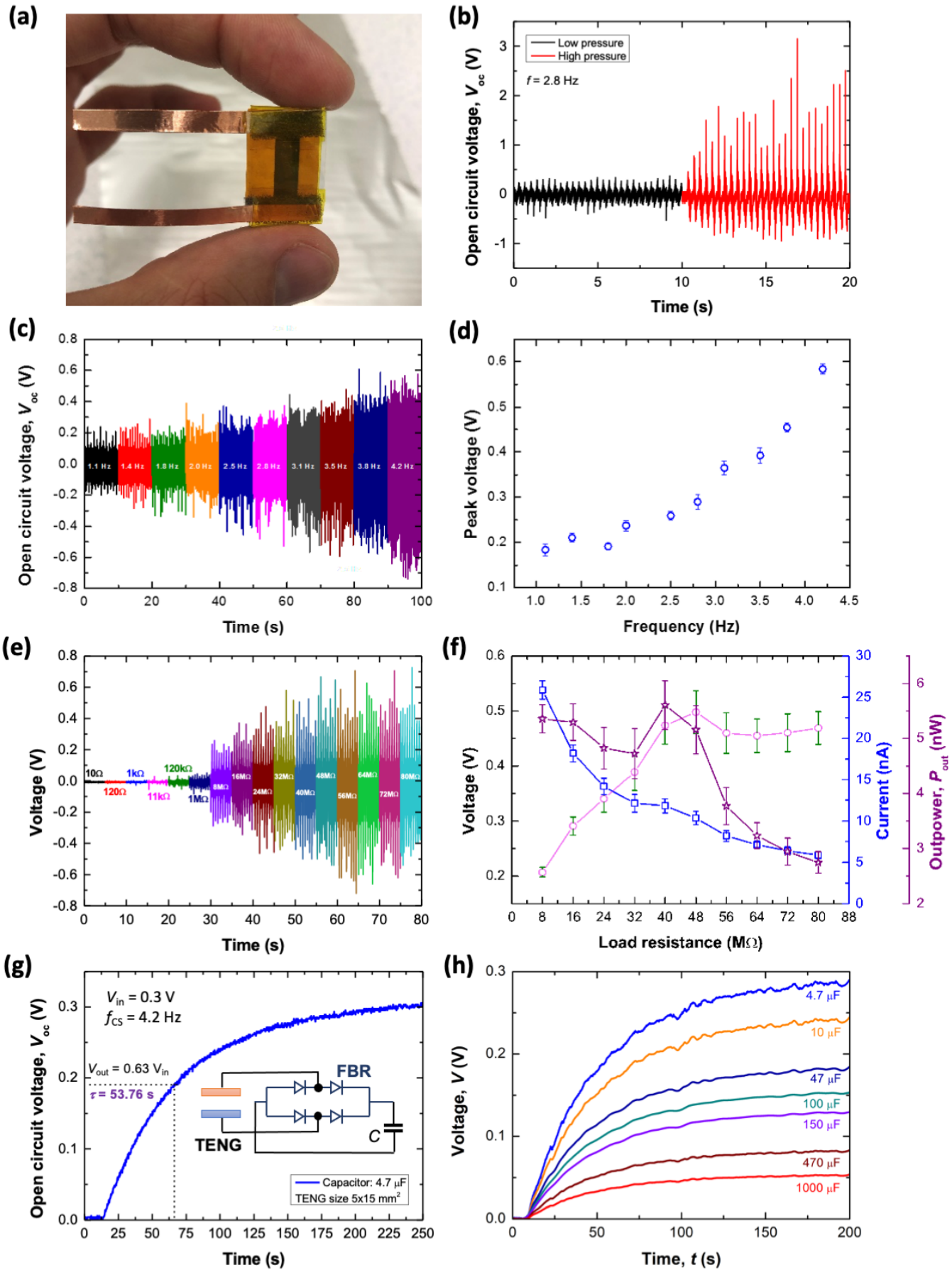

Figure 5. (a) Photograph of the miniaturised TENG with an effective 3DG area of 75 mm^2. (b) V_{oc} vs time for various contact-separation pressures, studying 13 kPa (*low pressure*) and 130 kPa (*high pressure*) at a constant contact-separation frequency of 2.8 Hz. (c) V_{oc} vs time, varying the contact-separation frequency between 1.1 to 4.2 Hz. (d) Peak voltage (V_p) extracted from (c) vs frequency. (e) Voltage produced by the TENG showed in (a) connected to an external R_{load}, @ 130 kPa and 4.2 Hz. (f) Voltage,

current and output power vs R_{load}. (g) Charging characteristic curve of a 4.7 μF capacitor charged by TENG device presented in (a); inset: electronic circuit used to transfer energy from TENG to a capacitor. (h) Comparison of charging curves obtained for various capacitors.

The V_{oc} of miniaturised TENG was characterised as a function of the pressure applied during the contact stage described in Figure 3. For that, low and high pressures of 13 and 130 kPa, respectively, have been tested. The study exhibits a clear increase of the peak voltage of around a factor 5 when high pressure is applied (Figure 5(b)). This result indicates the deformation behaviour of interfacial nanostructures existing in 3DG during the contact process. This deformation is expected to determine the pressure-voltage relationship of TENG, in good agreement with previous studies, where triboelectric charge density was improved by the contact surface between the triboelectric materials via nano-texturization of the surface leading to a drastic increase of the contact pressure [31]. The unique porous nanostructure of 3DG utilised in this TENG devices and presented in Figure 2(a3) (and Figure S3), offers a surface enlargement effect by interfacial nanostructure formation, preventing the use of any complex and costly lithography step. However, this condition is only observed when the applied pressing pressure is stronger than certain threshold pressure to make the full contact conditions. In our case, the comparison between low- and high-pressure conditions, evidenced that forces of 1 and 10 N applied to the 75 mm^2 area of our TENG, resulting in pressures of 13 and 130 kPa, both exhibiting energy generation, which indicates that the pressure threshold might be below that range. These results make our 3DG-TENG to be useful as energy harvesting from human body (i.e., breathing, heart beating, blinking, walking, running, typing, etc.) where applied pressures are demonstrated to be above 1 N range. Regarding the pressure range, studies reported in the literature indicated that low pressures around 16 kPa only reached 0.25% of the so-called *real* contact area in flat based TENG [32]. However, this real contact area could be enhanced towards 82% by increasing the pressure up to the MPa range (typically observed in mechanical energy produced by ocean waves). These numbers evidence that large dynamic range of contact-pressure that TENG device presents, keeping in mind that depending on the properties of the material, the utilisation of large pressure could lead to deterioration of material properties via material transfer or plastic deformation [33]. As we will present in following sections, we have tested 3DG-TENG under MPa range, observing great enhancement of the output characteristics, while preserving device stability and preventing material transfer.

Figure 5(c) presents the study of V_{oc} as a function of time for various frequencies ranging between 1.1 and 4.2 Hz. The results clearly indicate a drastic increase of the V_{oc} with the frequency from 0.18±0.02 V (@ 1.1 Hz) up to 0.58±0.02 V (@ 4.2 Hz), which is a factor 3 increase on the measured V_{oc}. The output signal of the TENG probes the sensitivity of the device voltage generation as a function of the frequency which makes the devices to be highly tuneable depending on the application. For example, human mechanical energy produced by breathing (0.1Hz), heart beating (0.6 Hz), blinking (1 Hz), walking (2 Hz), running (5 Hz), and typing (7 Hz), will produce voltages from few millivolts up to few volts, using the devices showed in Figure 5(a). This increase of V_{oc} with frequency experimentally observed in Figure 5(d) has not been explained by theoretical models such as DDM [34], and theoretical calculations of TENG output characteristics with frequency [35]. Triboelectricity mainly governed by electron [36], ion [37] and charged material transfer [38], has been observed here to be highly influenced by the separation of the triboelectric surfaces and the realising (distancing) speed achieved from the pressed stage (Figure 3). The increase of the frequency leads to a greater V_{oc} mainly due to the higher kinetic energy of the plates when they are brought in contact [35]. The deformation of the triboelectric material for certain values of applied pressures during the pressed stage, alters the electric field causing the charge transfer between electrodes. As such the product between the electric field across the dielectrics of the TENG and their thickness strongly depends on the applied pressure, the latter being dependent on the frequency. Further investigations of the working mechanism of TENG are needed in order to adapt the theoretical model to the experimental evidence. To demonstrate the relationship between pressed pressure (or contact pressure) and applied frequency, measurements have been carried out mounting a load cell in the equivalent position of one of the electrodes (Figure 4). The studies conclude that contact pressure increases with the frequency (*see* **Error! Reference source not found.**, Supplementary Material), justifying the observed increase not only in miniaturised 3DG-TENG presented in this section but also in larger-scale devices discussed later on.

The energy generation features of our 3DG TENGs have been evaluated by connecting the miniaturised device (Figure 5(a)) to an external load ranged between 10 Ω and 80 MΩ (Figure 5(e)). From those studies, one could conclude that there was a threshold in R_{load} above what the TENG started showing effective energy generation. In

other words, R_{load} above 1 MΩ exhibited a partial matching of electric impedance between the generator and the external load (Figure 5(e)). Further optimisation of the impedance between components, resulting in the minimisation of impedance mismatch for R_{load} above 40 MΩ, above what the voltage generated by the TENG showed a constant value of around 0.45-0.50 V. The I_{sc} of the same devices was measured by using an electrometer as a function of the same R_{load}, showing the opposite behaviour as the voltage. In good agreement with previous works reported on TENG [39,40], the I_{sc} decreases with R_{load}, mainly due to the increase of the voltage as the TENG internal impedance is matched with the external load (Figure 5(f)), well-known as Ohmic loss. Figure 5(f) summarises the voltage, current and output power generated by the TENG as a function of the R_{load}. From that figure, it is worth noting that there is an optimum R_{load} (40 MΩ) where TENG exhibited the best output power of 5.6 nW (i.e., 5.6 mW/m^2 power density), which set the best conditions for the TENG to be connected to external loads, e.g., energy storage devices, sensors, electronic devices, etc.

As we will demonstrate in the next section, scaling up the TENG device by increasing the area of the triboelectric materials, changes the internal impedance of the device, shifting the optimum R_{load} towards a different value. One of the main characteristics observed in our miniaturised TENG, that will be also evident in our large-scale TENG is the low R_{load} (range of tens of MΩ) compared to other reported works on graphene based TENG, exhibiting best P_{out} at R_{load} in the hundreds of MΩ (Table 1) [23]. The significant change in the internal impedance of our TENG makes this device to be a good energy generator, presenting low energy losses due to power dissipation, and reducing the use of complex power management boards [40]. TENG is well-known to have a large impedance and unbalanced load matching with external components. In this work, 3DG has been demonstrated to produce an inherent low impedance, simplifying their connectivity to external devices.

Despite its small size, our miniaturised 3DG TENG was tested as an energy generator to charge capacitors of different capacitances. Figure 5(g) illustrates the charging curve of a capacitor with a capacitance of 4.7 μF, charged with a miniaturised TENG working at 4.2 Hz. To charge this capacitor, the AC signal generated by the TENG was transformed into a DC signal using a full bridge rectifier (FBR) consisting of a diode bridge (*see* inset of Figure 5(g)). The experiment probed the successful charge of a small capacitor, achieving saturation voltages of 0.3 V with charging times around 53.75s. The charging time was calculated from the input voltage (V_{in}) of 0.3 V, and the time TENG takes to charge 63% of the V_{in}. This method has been used to compare the charging time produced by these small TENG devices to charge capacitors with capacitances ranged between 4.7 μF to 1 mF. Figure 5(h) summarises the comparison of all the charging curves. One could conclude from that figure that the miniaturised TENG is capable to charge rapidly small capacitors with values of 4.7 μF (τ = 56 s) and 10 μF (τ = 94 s), exhibiting more difficulties to reach V_{in} as the capacitance of the capacitors increases (e.g., 47 μF with τ = 398 s, or 100 μF with τ > 500 s). This is not necessarily a negative feature, as the miniaturised TENG could be used as an active component in boosted TENG configurations, where two or more TENGs are connected in series to enhance the performance of the devices through a feeding process. In that configuration, small capacitors charge larger ones (*cascade structure*). In that scenario, small TENG like the one developed here could be used to provide charges to the small capacitors, being part of a larger power generation system [41].

3.2 Large scale 3DG based TENG

3.2.1 Study of frequency and triboelectric electrodes gap distance

The role of the frequency and electrodes maximum gap distance (d_{gap}) in TENG devices working in contact-separation mode (Figure 3), was tested in larger devices than those discussed in the former section. In this study, TENG devices with an effective area of 16 cm^2 were characterised using the setup described in Figure 4. Figure 6(a) presents the V_{oc} measured for different frequencies ranged from 50 mHz to 4 Hz. From that figure, one could easily observe that V_{oc} increases with the frequency, in good agreement with the results obtained in miniaturised devices Figure 5(c). For example, the frequencies 50 mHz and 4 Hz produced V_{oc} of 26 ± 5 V and 285 ± 7 V, respectively. This increase was observed for threshold values of frequency above 0.2 Hz, exhibiting a drastic enhancement of V_{oc} for frequencies above 1 Hz. From that figure, one could also observe that the positive and negative peak voltages do not reach the same values, making TENG output characteristics be asymmetric. This feature must be considered during the integration of this energy sources to external circuits and power management modules. For the sake of

clarity, Figure 6(b) shows the mean of the peak-to-peak voltages, and their standard error, extracted from Figure 6(a), and called here V_{oc}. In this figure, a linear regression of the experimental data is observed following a function V_{oc} = 230 V·s * f (Hz) @ frequencies below 1 Hz. This function allows the tunability of the TENG working regime, depending on either the application electric energy requirements or mechanical energy frequency. Above frequencies of 1 Hz, a saturation of the V_{oc} values is observed, indicating that frequencies around 3 Hz have a positive effect on $V_{oc,}$ producing maximum V_{oc} values ranged between 275-300 V, leading to a more efficient transport of positive and negative charges to the electrodes of the TENG (*see* schematic in Figure 3). That means, the faster the electrodes separate, the more carrier density with oppositive charge is accumulated in the electrodes of the TENG, and thus, the higher electric field is built during the separation stage. Similar effect is observed during the approaching stage.

As a result, the peak-to-peak voltage, or called here V_{oc} increases with the frequency (Figure 6(b)). However, this mechanism exhibited a maximum, and a decay for frequencies above 3 Hz is observed. That decrease of the V_{oc} for frequencies > 3 Hz is in good agreement with the study of the pressure as a function of the applied frequency (*see* **Error! Reference source not found.** in Supplementary Material) and partially support the idea of a system effect instead of a material effect. In our described setup and device structure, results demonstrated an optimum contact pressure reached at applied frequencies around 3 Hz, which is in good agreement with the V_{oc} graph showed in Figure 6(b). Since DDM does not predict effect of the frequency on the V_{oc}, and from our observations obtained in this study, we conclude frequency is a parameter characteristic of the setup or actuation system used to excite TENG.

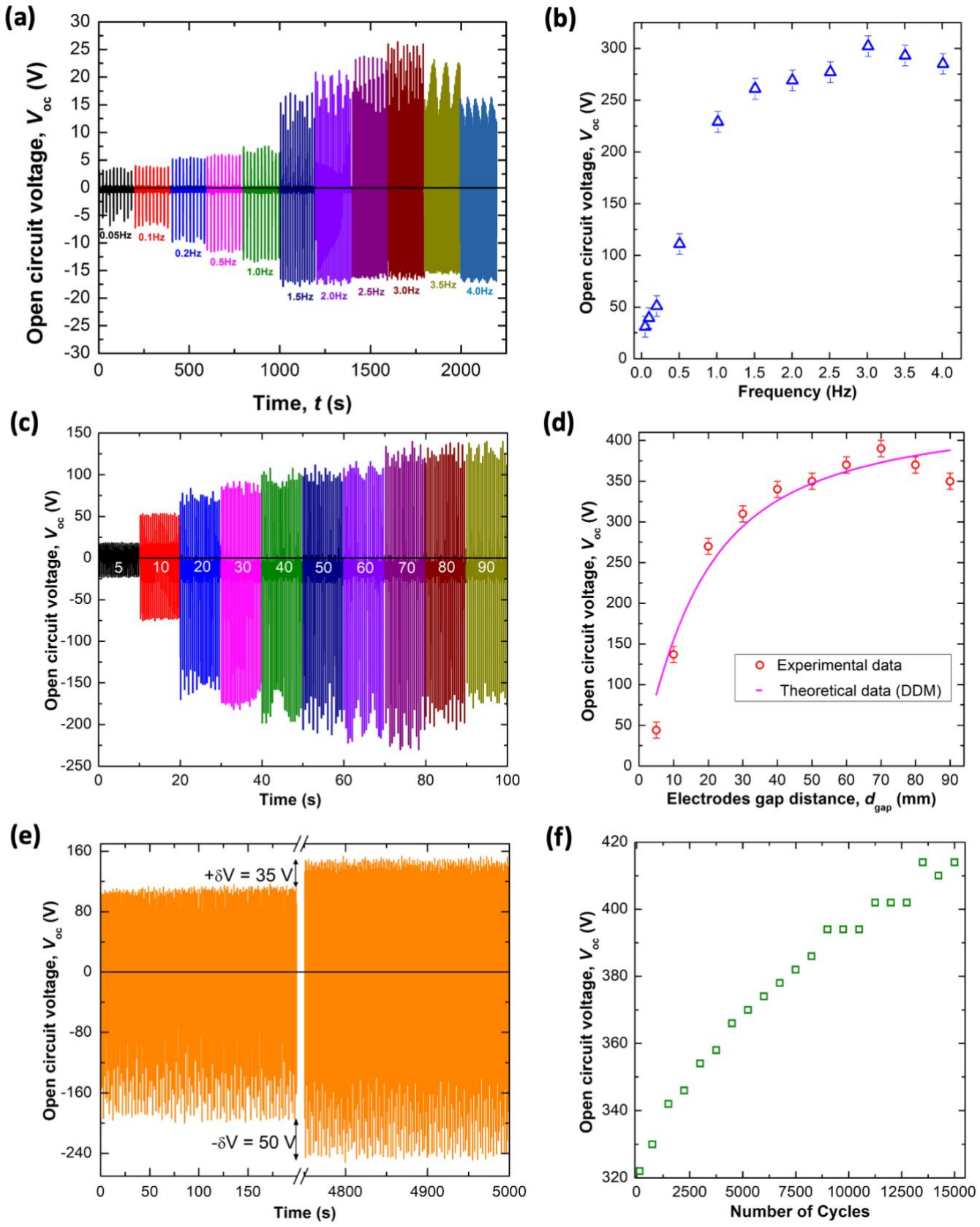

Figure 6. Characterisation TENG devices with an effective area of 16 cm^2. (a) V_{oc} vs time for various frequencies. (b) V_{oc} vs frequency extracted from (a) (*blue triangles*). (c) V_{oc} vs time for different electrodes gap distances (expressed in mm). (d) V_{oc} vs electrodes gap distance extracted from (c) (*red circles*) and simulations (*pink line*). (e) Stability cyclic test measured in 3DG-TENG at a frequency of 3 Hz and d_{gap} = 70 mm. (f) V_{oc} vs number of contact-separation cycles; extracted from (e).

Figure 6(c) presents the results obtained for V_{oc} measured as a function of the electrode gap distance. This distance corresponds to the maximum distance achieved during the separation stage of the experiment. From this study two conclusions emerge: i) V_{oc} increases with d_{gap} and ii) V_{oc} exhibits maximum values at d_{gap} of 70 mm, showing a

reduction of the V_{oc} for distances above that value. This result indicates that the electric field between electrodes highly depends on the distance between them, as supported by the DDM [34], and finite element analysis [42], where V_{oc} is expected to increase with d_{gap}. By increasing the distance between electrodes, the electric field is reduced for the same electric potential. From Figure 6(b), one could understand that at d_{gap} < 70 mm, the decrease of the electric field due to the increase of d_{gap} is overcompensated by the time left to the charges to accumulate at each electrode, resulting in a net increase of V_{oc}. For d_{gap} < 70 mm, maximum charge density accumulated at the electrodes was reached, d_{gap} being the only factor limiting V_{oc}. This influence of gap distance on the V_{oc} has been also interpreted using an electric equivalent circuit [42], where V_{oc} depends inversely on the capacitance of the triboelectric electrodes; in that regard, the increase of the d_{gap} produces a decrease of the capacitance between the electrodes, leading to an increase of the V_{oc}.

Figure 6(d) includes the experimental values of V_{oc} (obtained from Figure 6(c)) as a function of d_{gap} along with the fitting values simulated by the DDM. This model was fitted to the experimental measurements, aiming to obtain a variety of σ_T values for ε_{3DG} ranged between $2\varepsilon_0$ and $8\varepsilon_0$, resulting in σ_T values ranged from 0.890 mC/m^2 to 1.704 mC/m^2, respectively (*see* complete list of simulations in **Error! Reference source not found.**, Supplementary Material). For every value of ε_{3DG} tested, a residual error (R^2) of around 0.95 was obtained. For comparison, MXene-3DG TENG obtain a maximum σ_T value of 0.150 mC/m^2 [43] which is one order of magnitude lower σ_T than those obtained with our 3DG. This method allowed the indirect estimation of σ_T by using DDM and experimental values of V_{oc}. DDM could be also used to predict I_{sc} using the calculated σ_T and the DDM expressions for I_{sc} expressed as a function of the gap distance and triboelectric properties of materials. **Error! Reference source not found.** (Supplementary Material) presents the characteristic I_{sc} peak for the 3DG TENG.

The excellent fitting of the model with the experimental data confirms the relationship between the V_{oc} and the distance between electrodes, exhibiting a stable output response in voltage of the 3DG-TENG for gaps above 40 mm. However, the experimental results exhibited a V_{oc} for gaps above 70 mm, which was not predicted by DDM. In order to find the reason for that unpredicted behaviour, we have also evaluated the influence of the gap on the applied pressure. For that, and similarly to the frequency study presented in **Error! Reference source not found.**, a load cell has been utilised to test the relationship between both parameters. **Error! Reference source not found.** presents the results of the study, where one could clearly observe a clear dependence of the applied pressure with the gap used during contact-separation experiments. Results evidence a maximum pressure achieved at 70 mm which matches well with the maximum V_{oc} showed in Figure 6(d). In conclusion, the TENG tester setup is governing the V_{oc} drop at higher gaps over the electrostatic induction effect explained by the DDM. Further experiments will be needed to determine the behaviour of the TENG at higher gaps, and to differentiate between the system and material components.

3.2.2 Stability cyclic study of TENG

The stability of the TENG output characteristics have been evaluated by subjecting TENG devices to 15,000 contact-separation cycles at a frequency of 3 Hz, and d_{gap} = 70 mm (Figure 6(e)). These operational parameters have been chosen because they presented the best device performance (Figure 6(b,d)). Results indicate that V_{oc} increases over time, i.e., the amplitude of the voltage generated by the TENG is greater with the number of cycles (Figure 6(f)). This observation agrees with previous results reported in the literature suggesting that TENG devices require a number of cycles to 'warm-up', i.e., to reach a constant triboelectric charge density at the triboelectric materials [30]. The time that a TENG needs to reach the steady-state stage not only depends on the triboelectric materials, but also on the frequency, applied pressure, and electrodes distance.

This makes the determination of the warm-up period a characteristic of the TENG design/materials and experimental conditions. Our TENG exhibited a unique feature that - to the best of our knowledge – has not been observed yet. Conventional TENG typically reaches saturated V_{oc} after few contact-separation cycles (within minutes time, depending on the applied frequency). In contrast, Figure 6(e) and (f) clearly highlight the non-steady performance of our 3DG-TENG, exhibiting a clear increase of the V_{oc} within the window of analysis. Moreover, from Figure 6(e), it can be concluded that max and min voltages increase around 35 and 50 V, respectively, after thousands of contact-separation cycles. This is even more evident in the Figure 6(f) extracted from (e), where TENG output voltage does

not show saturation. The constant increase of the V_{oc} from 320 V (first few contact-separation cycles) up to 416 V (after 15k cycles), being a factor 1.3 increase.

Another observation that we can make here is about the stability of the material. During long lasting cyclic test, material transfer from one electrode to the second one due to several contact-separation cycles, could hinder the stability of the TENGs. Figure 6(f) probes a great level of stability in our devices with a positive creation of voltage over time. Other works using CVD graphene and polyimides as triboelectric materials, did show a worst performance, exhibiting decrease about 5.1% in the V_{oc} after only 1,000 contact-separation cycles, and a dramatic decrease of V_{oc} by 56.3% after 1,300 cycles [44]. The absence of saturation and great material stability makes this 16 cm^2 3DG-TENG a very promising mechanical energy harvester in terms of output characteristics.

3.2.3 Characterisation of 3DG TENG as an energy source for energy storage devices

Figure 6(a-d) demonstrates operate the TENG devices at optimum conditions. As such, operating the TENG devices with a frequency of 3 Hz and a gap distance of 70 mm, the output power generated by the TENG has been evaluated (Figure 7(b)). To that end, voltage and current have been measured as a function of the R_{load} ranged between 120kΩ and 240 MΩ. Figure 7(b) presents the summary of the obtained results, where voltage has been obtained from Figure 7(a). In that figure, three conclusions can be made: i) the peak-to-peak voltage exhibited a transition between tens of volts measured at R_{load} < 10 MΩ and 250 V measured at R_{load} > 100 MΩ; ii) the current exhibited the opposite transition, with high currents of 150 μA measured at R_{load} < 10 MΩ and low currents of tens of μA measured at R_{load} > 300 MΩ; iii) the output power showed a maximum value of around 10.37 W/m^2 at R_{load} around 40 MΩ. Compare with other carbon nanostructures based TENG, 3DG presents higher output powers per unit of area and weight (*see* Table 1).

For example, CNT based TENG demonstrated P_{out} of 8 W/m^2 [22] being a factor 1.4 lower than that obtained here. Comparing our CVD 3DG with other graphene synthesised by techniques such as laser induced processes, results also indicate a drastic improvement of the P_{out} from 2.36-3.06 W/m^2 [24] to 10.37 W/m^2 that we demonstrated in this work. Moreover, CVD technique has demonstrated to produce a lower internal impedance graphene foam, compared to laser induce graphene (LIG) [24] and shear exfoliated graphene (SEG) [23], with low R_{load} of 40 MΩ exhibiting the maximum P_{out} compared to other synthesis techniques, resulting in large internal impedances, requiring thus larger R_{load} of 70 and 200 MΩ for LIG and SEG, respectively. In contrast, crumble graphene has demonstrated record values of low internal resistance, with R_{load} of 2 MΩ to produce maximum output powers. However, that output power was observed to be orders of magnitudes below those reported here (i.e., 0.0025 W/m^2) [25].

Large TENG has been tested as an energy source to charge capacitors of different capacitances ranged between 9.3 μF and 86.5 μF. Figure 7(c) presents the characteristic curves of these capacitors charged by our large 3DG TENG operated at 3 Hz and using a d_{gap} of 70 mm. Similar to the case of the miniaturised 3DG TENG presented in Figure 5(g), TENG was connected to a capacitor through a FBR. The result of the study demonstrates an enhanced performance in 3DG TENG charging low capacitance capacitors, e.g., 9.3 μF, exhibiting a saturation voltage of around 7 V (i.e., 100% of the input voltage or also called here V_{in}) in less than 30 s. As the capacitance of the energy storage devices increased, the TENG devices needed more time to reach the saturation level. For the sake of comparison, at 200 s, TENG was able to reach 92.85% and 78.57% of the V_{in}.

These enhanced values were obtained by using the R_{load} of 40 MΩ optimised in (Figure 7 (a,b)). The connected in series with the R_{load} demonstrated to be a good energy source for charging the capacitor, the absence of this load resistor hindering the charging time (Figure 7 (d)). This result evidences the high internal impedance of TENG devices, already suggested in the literature [15], making their integration in external circuits challenging. As such their associated energy losses are one of the main drawbacks to be addressed [45,46]. Further studies comprising the dry/wet treatment of 3DG to tune its work function are expected to reduce R_{load} needed to obtain the maximum P_{out}.

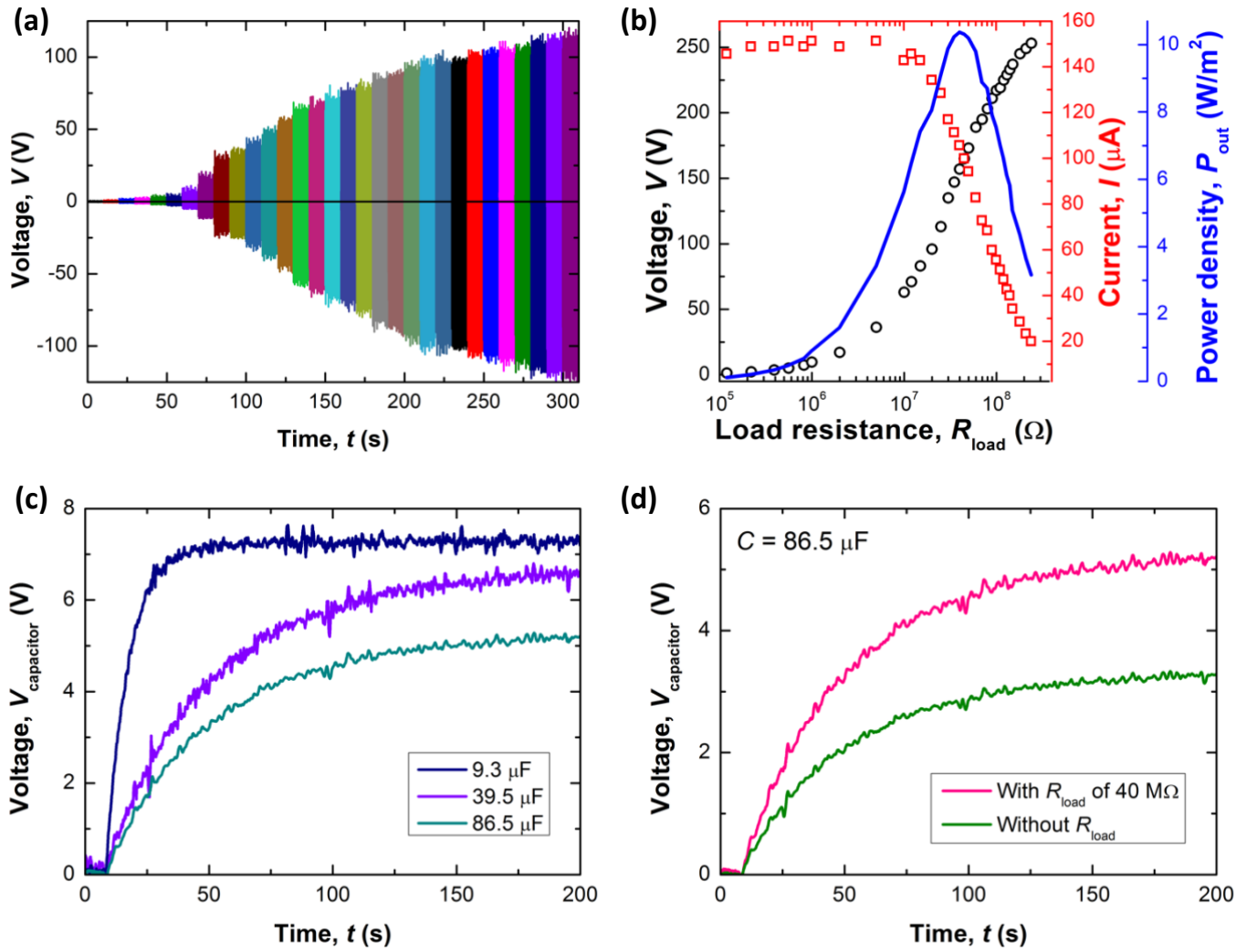

Figure 7. Characterisation TENG devices with an effective area of 75 cm^2. (a) TENG voltage vs time for various R_{load} (from *left* to *right*: 120kΩ, 220kΩ, 390kΩ, 560kΩ, 820kΩ, 1MΩ, 2MΩ, 5MΩ, 10MΩ, 12MΩ, 15MΩ, 20MΩ, 25MΩ, 30MΩ, 35MΩ, 40MΩ, 45MΩ, 5MΩ, 60MΩ, 70MΩ, 80MΩ, 90MΩ, 100MΩ, 110MΩ, 120MΩ, 130MΩ, 140MΩ, 150MΩ, 180MΩ, 210MΩ, and 240MΩ). (b) TENG characteristics, including V_{pp}, I and P_{out} vs R_{load} extracted from (a). (c) Characteristic curves of 9.3, 39.5 and 86.5 μF capacitors charged by using TENG @ 3 Hz and d_{gap} of 70 mm, and a R_{load} resistor of 40 MΩ. (d) Characteristic curves of 86.5 μF capacitor charged by a TENG @ 3 Hz and d_{gap} of 70 mm with and without using a R_{load} resistor of 40 MΩ.

3.2.4 Autonomous pressure sensors based on TENG

3DG-TENG has been tested as an autonomous pressure sensor for room occupancy monitoring. For this application a 4×1 array of sensors has been assembled in a light-weight mat (Figure 8(a)). Each pressure sensor was connected to the analog ports of an Arduino Mega, using a voltage divider to adjust the maximum voltage generated by the sensors to the max input voltage accepted by the microcontroller (i.e., 5 V). That strategy has been proved here to be an effective method to prevent crosstalk between sensors, increasing their signal-to-noise ratio and thus improving the recognition of people preventing the use of signal filtering. An algorithm programmed in Labview allowed to measure the voltage generated by each sensor and to display the results in real-time (*see* logic diagram in Figure 8(b)). The algorithm was capable of: i) identifying people anonymously based on measuring their unique temporal pressure profile, ii) counting number of people entering/leaving the room, and iii) recognising if the person was entering or leaving the room. These features offered by the mat are particularly useful to detect unauthorised people intrusions in restricted areas. In addition, occupancy can be used to optimise active aircon, radiator temperature, windows ventilation, etc to improve the air quality in rooms maximum limits. As such this mat could play a major role in optimising energy resources of buildings and houses towards a more sustainable planet.

Experimental results included in Figure 8 demonstrated that TENG could be used for dynamic pressure sensors in good agreement with previous theoretical works reported in the literature [47]. The key feature of this self-powered mat is the identification of people anonymously, utilising the characteristic pattern generated by the 3DG TENG output voltage, without the need of an external energy source. The experiment presented in Figure 8(c-e) and in the Videos 4-6 of the Supplementary Material, show three people with different weights and wearing different shoes/trainers, producing characteristic patterns on the pressure mat (Figure 8(d)). The four sensors used in the current version of the mat, allow to gather enough information to detect different people, firstly, through the peak voltage generated by the TENG, which is characteristic of the applied contact pressure (i.e., the more weight the more peak voltage); secondly from the secondary peaks which are generated by the partial release of the 3DG-PET contact observed during the realising stage. Furthermore, the secondary peaks observed in Figure 8 are expected to give a detailed information about the way a person walks/runs, since these sub-peaks evidence alternative contact-separation directions than standard vertical mode. In this scenario, the mat and further analysis of the secondary peaks will be promising for improving the technique of sport professionals (e.g., golfers, runners, etc.)

As demonstrated in **Error! Reference source not found.**, TENG sensors present great sensitivity to pressure, making them excellent candidates to detect anonymously different people entering rooms, buildings, restricted areas, etc. For that, the separators of the TENG device could be adapted to the region pressures one wants to sense. In this work, we have used highly compressed foam (90 kg/m^3), bringing the level of sensitivity to the kPa-MPa expected to be exerted by ground pressure of a human foot on the mat (kPa: human walking; MPa: spike heels). **Error! Reference source not found.** presents the V_{oc} measured as a function of the pressure applied on TENG devices used in the pressure mat in Figure 8. Using the same configuration and setup utilised in **Error! Reference source not found.**, the sensitivity (S) of TENG has been tested applying pressures ranged between 1 Pa to 10 MPa. That range of pressures covers from a light touch applied by a human hand on the mat, to a hard pressure applied by a human waking on the mat in heels. The highly compressed foam used for the TENG, places the highest sensitivity of the sensors at pressure ranged between 1-10 kPa, exhibiting a sensitivity (S) of around 9.4±0.3 V/Pa. This is the most conventional scenario considering people wearing trainers and shoes. Sensitivity of these sensors decreases by an order of magnitude (0.42±0.02 V/Pa) at applied pressures above 10 kPa. That makes these TENG still useful to detect pressures in the MPa range but with less sensitivity.

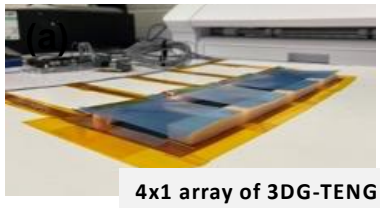

4x1 array of 3DG-TENG

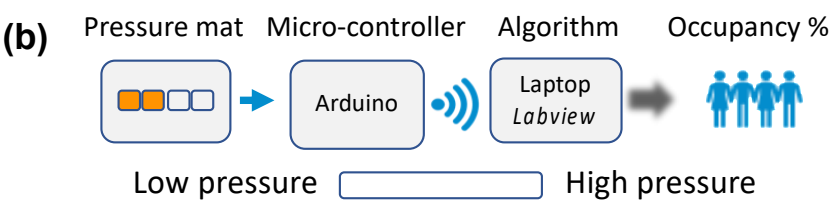

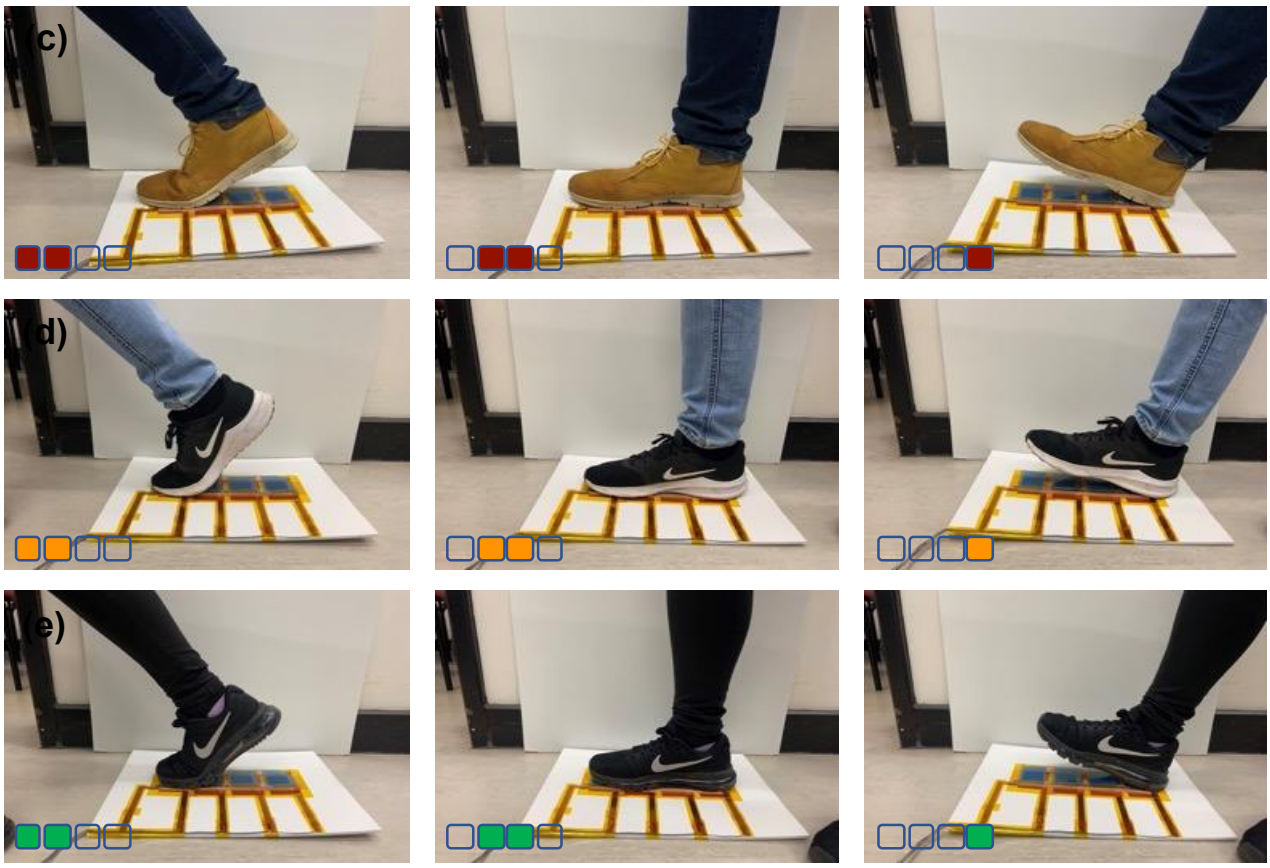

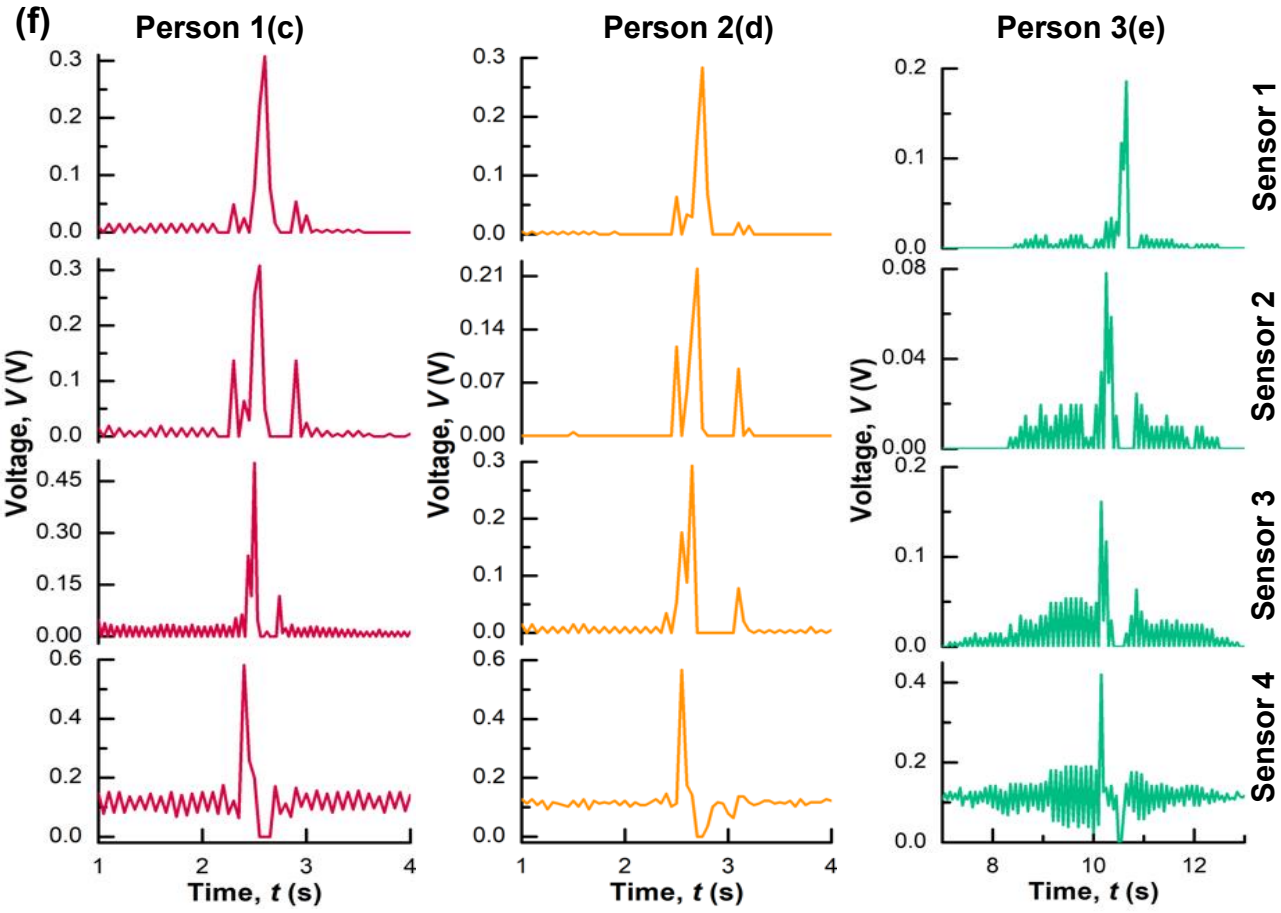

Figure 8. (a) Photograph of self-powered pressure mat based on 4×1 array of 3DG-TENG. (b) Logic diagram of the data acquisition, communication, and analysis of mat readings for occupancy monitoring. Photo-frames of person 1(c), 2(d) and 3(e) walking on the pressure mat. (f) Characteristic pressure patterns generated by each person when sensors 1-4 were pressed.

4. Conclusions

This work demonstrates the successful use of 3DG foam as a tribopositive electrode in TENG, exhibiting high P_{out} of around 10.37 W/m^2 which are record values for carbon based TENG. These values were achieved by using a load resistance of 40 MΩ being an order of magnitude lower than that needed with other variations of graphene based TENG. These results evidenced a low internal impedance exhibited by the 3DGii^{TM}, facilitating the integration of 3DG-TENG with external integrated circuits (IC), printable and wearable electronics, and CMOS technology for near future IoT.

The thorough study of 3DG-TENG output characteristics as a function of frequency, electrodes gap and applied pressure concluded that porous structure of 3DG benefited the charge transfer while minimising energy loss. 3DG-TENG demonstrated great stability and low material transfer over 15,000 of cyclic mechanical stimulus, preserving almost 100% of the initial output power. This effect exhibited a factor 5 increase of the V_{oc} when the applied pressure between electrodes was increased, probing that 3DGii^{TM} material has a great density of interfacial nanostructures, making this material to be more comprisable that other variants of graphene. This feature demonstrated an enhancement of the output characteristics while preserving the mechanical properties of the 3DG film. In this work, the distance dependent model was used for the first time to estimate a σ_T of around 0.890 - 1.704 mC/m^2, being an order magnitude higher than that obtained for other graphene variants. This high surface charge density reached by 3DG upon contact-separation with PET, being the main responsible for the record values of P_{out} observed in this work.

Taking advantage of the exceptional performance of 3DG-TENG, these devices were successfully utilised to charge energy storage devices. Moreover, 3DG-TENG was tested as self-powered sensors in an energy-autonomous pressure sensitive mat. 3DG-TENGs have demonstrated great sensitivity to pressure, allowing the fabrication of a pressure mat to anonymously identify people entering/leaving a room, and probing the validity of these devices for dynamic pressure sensing. The pressure sensing platform based on autonomous 3DG-TENG array, opens up promising matters of investigation in fields such as elite sports and performance enhancement, health treatments, and sustainable use of energy resources in smart buildings and cities.

CRediT authorship contribution statement

Emma Keel: Conceptualization, methodology, software, validation, investigation, formal analysis, and writing (original draft preparation); **Ammara Ejaz:** Methodology, TENG characterisation; **Michael McKinlay:** TENG modelling and formal analysis. **Manel Pelayo:** TENG characterisation and formal analysis; **Marco Caffio:** Supervision, and project administration; **Des Gibson:** Supervision, project administration, and writing (review and editing); **Carlos García Núñez:** Methodology, formal analysis, supervision, project visualisation and administration, and writing (original draft preparation, review and editing). All authors have read and agreed to the published version of the manuscript.

Declaration of Competing Interest

The authors declare that they have no known competing financial interests or personal relationships that could have appeared to influence the work reported in this paper.

Data availability

Data will be made available on request.

Acknowledgements

The authors are grateful for financial support from Scottish Research Partnership in Engineering (NMIS/IDP-011) and British Council & Higher Education Commission (20-ICRG-165/RGM/HEC/2020).

References

[1] L. Liu, X. Guo, C. Lee, Promoting smart cities into the 5G era with multi-field Internet of Things (IoT) applications powered with advanced mechanical energy harvesters, Nano Energy. 88 (2021) 106304. https://doi.org/10.1016/J.NANOEN.2021.106304.

[2] M.H. Miraz, M. Ali, P.S. Excell, R. Picking, A review on Internet of Things (IoT), Internet of Everything (IoE) and Internet of Nano Things (IoNT), Internet Technologies and Applications (ITA), Proc. 6th Int. Conf. (2015) 219–224. https://doi.org/10.1109/ITECHA.2015.7317398.

[3] C. Qiu, F. Wu, C. Lee, M.R. Yuce, Self-powered control interface based on gray code with hybrid triboelectric and photovoltaics energy harvesting for IoT smart home and access control applications, Nano Energy. 70 (2020) 104456. https://doi.org/10.1016/J.NANOEN.2020.104456.

[4] X. Pu, W. Hu, Z.L. Wang, Toward wearable self-charging power systems: the integration of energy-harvesting and storage devices, Small. 14 (2018) 1702817. https://doi.org/10.1002/SMLL.201702817.

[5] C. García Núñez, L. Manjakkal, R. Dahiya, Energy autonomous electronic skin, npj Flexible Electronics 3 (2019) 1–24. https://doi.org/10.1038/s41528-018-0045-x.

[6] J. Pan, J. McElhannon, Future edge cloud and edge computing for internet of things applications, IEEE Internet Things J. 5 (2018) 439–449. https://doi.org/10.1109/JIOT.2017.2767608.

[7] F.R. Fan, Z.Q. Tian, Z. Lin Wang, Flexible triboelectric generator, Nano Energy. 1 (2012) 328–334. https://doi.org/10.1016/J.NANOEN.2012.01.004.

[8] G. Zhu, B. Peng, J. Chen, Q. Jing, Z. Lin Wang, Triboelectric nanogenerators as a new energy technology: from fundamentals, devices, to applications, Nano Energy. 14 (2015) 126–138. https://doi.org/10.1016/J.NANOEN.2014.11.050.

[9] S. Wang, L. Lin, Z.L. Wang, Triboelectric nanogenerators as self-powered active sensors, Nano Energy. 11 (2015) 436–462. https://doi.org/10.1016/J.NANOEN.2014.10.034.

[10] S. Niu, Z.L. Wang, Theoretical systems of triboelectric nanogenerators, Nano Energy. 14 (2015) 161–192. https://doi.org/10.1016/J.NANOEN.2014.11.034.

[11] Z.L. Wang, T. Jiang, L. Xu, Toward the blue energy dream by triboelectric nanogenerator networks, Nano Energy. 39 (2017) 9–23. https://doi.org/10.1016/J.NANOEN.2017.06.035.

[12] A. Ahmed, I. Hassan, M.F. El-Kady, A. Radhi, C.K. Jeong, P.R. Selvaganapathy, J. Zu, S. Ren, Q. Wang, R.B. Kaner, Integrated triboelectric nanogenerators in the era of the Internet of Things, Adv. Sci. 6 (2019) 1802230. https://doi.org/10.1002/ADVS.201802230.

[13] C. Fang, T. Tong, T. Bu, Y. Cao, S. Xu, Y. Qi, C. Zhang, Overview of power management for triboelectric nanogenerators, Adv. Int. Sys. 2 (2020) 1900129. https://doi.org/10.1002/AISY.201900129.

[14] R. Walden, C. Kumar, D.M. Mulvihill, S.C. Pillai, Opportunities and challenges in triboelectric nanogenerator (TENG) based sustainable energy generation technologies: a mini-review, Chem. Eng. J. Adv. 9 (2022) 100237. https://doi.org/10.1016/J.CEJA.2021.100237.

[15] Z. Zhang, D. Jiang, J. Zhao, G. Liu, T. Bu, C. Zhang, Z. Lin Wang, Z. Zhang, D. Jiang, J. Zhao, G. Liu, T. Bu, C. Zhang, Z.L. Wang, Tribovoltaic effect on metal–semiconductor interface for direct-current low-impedance triboelectric nanogenerators, Adv. Energy Mater. 10 (2020) 1903713. https://doi.org/10.1002/AENM.201903713.

[16] H. Wang, M. Han, Y. Song, H. Zhang, Design, manufacturing and applications of wearable triboelectric nanogenerators, Nano Energy. 81 (2021) 105627. https://doi.org/10.1016/J.NANOEN.2020.105627.

[17] T. Kim, J. Chung, D.Y. Kim, J.H. Moon, S. Lee, M. Cho, S.H. Lee, S. Lee, Design and optimization of rotating triboelectric nanogenerator by water electrification and inertia, Nano Energy. 27 (2016) 340–351. https://doi.org/10.1016/J.NANOEN.2016.06.051.

[18] J. Yeong Park, M. Salauddin, M. Salauddin Rasel -, E. Zhao, K. Jiang, B. Li, al -, F. Yuan, S. Liu, J. Zhou, W. Tang, T. Zhou, C. Zhang, F. Ru Fan, C. Bao Han, Z. Lin Wang, A power-transformed-and-managed triboelectric nanogenerator and its applications in a self-powered wireless sensing node, Nanotechnology. 25 (2014) 225402. https://doi.org/10.1088/0957-4484/25/22/225402.

[19] Y.S. Choi, S.-W. Kim, S. Kar-Narayan, Y.S. Choi, S. Kar-Narayan, -W S Kim, Materials-related strategies for highly efficient triboelectric energy generators, Adv. Energy Mater. 11 (2021) 2003802. https://doi.org/10.1002/AENM.202003802.

[20] R.D.I.G. Dharmasena, K.D.G.I. Jayawardena, C.A. Mills, R.A. Dorey, S.R.P. Silva, A unified theoretical model for triboelectric nanogenerators, Nano Energy. 48 (2018) 391–400. https://doi.org/10.1016/J.NANOEN.2018.03.073.

[21] F.F. Hatta, | Muhammad, A. Shazni, M. Haniff, | Mohd, A. Mohamed, T. Mara, C. Selangor, A review on applications of graphene in triboelectric nanogenerators, Int. J. Energy Res. 46 (2022) 544–576. https://doi.org/10.1002/ER.7245.

[22] M. Matsunaga, J. Hirotani, S. Kishimoto, Y. Ohno, High-output, transparent, stretchable triboelectric nanogenerator based on carbon nanotube thin film toward wearable energy harvesters, Nano Energy. 67 (2020). https://doi.org/10.1016/j.nanoen.2019.104297.

[23] I. Domingos, A.I.S. Neves, M.F. Craciun, H. Alves, Graphene based triboelectric nanogenerators using water based solution process, Front. Phys. 9 (2021) 603. https://doi.org/10.3389/FPHY.2021.742563/BIBTEX.

[24] M.G. Stanford, J.T. Li, Y. Chyan, Z. Wang, W. Wang, J.M. Tour, Laser-induced graphene triboelectric nanogenerators, ACS Nano. 13 (2019) 7166–7174. https://doi.org/10.1021/acsnano.9b02596.

[25] H. Chen, Y. Xu, J. Zhang, W. Wu, G. Song, Enhanced stretchable graphene-based triboelectric nanogenerator via control of surface nanostructure, Nano Energy. 58 (2019) 304–311. https://doi.org/10.1016/J.NANOEN.2019.01.029.

[26] H. Chen, Y. Xu, L. Bai, Y. Jiang, J. Zhang, C. Zhao, T. Li, H. Yu, G. Song, N. Zhang, Q. Gan, Crumpled graphene triboelectric nanogenerators: smaller devices with higher output performance, Adv. Mater. Technol. 2 (2017). https://doi.org/10.1002/admt.201700044.

[27] F. Zhang, C. Klein, E. Longhi, S. Barlow, S.R. Marder, G. Sarusi, A. Kahn, Molecular-Reductant-Induced Control of a Graphene−organic interface for electron injection, Chem. Mater. 31 (2019) 6624-6632. https://doi.org/10.1021/acs.chemmater.9b00566.

[28] Gii material, registered by Integrated Graphene Ltd., (2016). https://www.integratedgraphene.com/gii-technology (accessed February 23, 2023).

[29] C. Douglas, C. García Nuñez, M. Caffio, D. Gibson, Ultra-thin graphene foam based flexible piezoresistive pressure sensors for robotics, Trans. Tech. Publ. (2022) 79–86. https://doi.org/10.4028/p-oy94hj.

[30] M.L. Seol, J.W. Han, D. il Moon, M. Meyyappan, Hysteretic behavior of contact force response in triboelectric nanogenerator, Nano Energy. 32 (2017) 408–413. https://doi.org/10.1016/J.NANOEN.2016.12.055.

[31] M.L. Seol, S.H. Lee, J.W. Han, D. Kim, G.H. Cho, Y.K. Choi, Impact of contact pressure on output voltage of triboelectric nanogenerator based on deformation of interfacial structures, Nano Energy. 17 (2015) 63–71. https://doi.org/10.1016/J.NANOEN.2015.08.005.

[32] G. Min, Y. Xu, P. Cochran, N. Gadegaard, D.M. Mulvihill, R. Dahiya, Origin of the contact force-dependent response of triboelectric nanogenerators, Nano Energy. 83 (2021) 105829. https://doi.org/10.1016/J.NANOEN.2021.105829.

[33] X. Xia, H. Wang, H. Guo, C. Xu, Y. Zi, On the material-dependent charge transfer mechanism of the contact electrification, Nano Energy. 78 (2020) 105343. https://doi.org/10.1016/J.NANOEN.2020.105343.

[34] R.D.I.G. Dharmasena, K.D.G.I. Jayawardena, C.A. Mills, R.A. Dorey, S.R.P. Silva, A unified theoretical model for triboelectric nanogenerators, Nano Energy. 48 (2018) 391–400. https://doi.org/10.1016/J.NANOEN.2018.03.073.

[35] B. Yang, W. Zeng, Z.-H. Peng, S.-R. Liu, K. Chen, X.-M. Tao, B. Yang, W. Zeng, Z.-H. Peng, S.-R. Liu, K. Chen, X.-M. Tao, A fully verified theoretical analysis of contact-mode triboelectric nanogenerators as a wearable power source, Adv. Energy Mater. 6 (2016) 1600505. https://doi.org/10.1002/AENM.201600505.

[36] C. Liu, A.J. Bard, Electrostatic electrochemistry at insulators, Nat. Materials 7 (2008) 505–509. https://doi.org/10.1038/nmat2160.

[37] L.S. McCarty, G.M. Whitesides, Electrostatic charging due to separation of ions at interfaces: contact electrification of ionic electrets, Angew Chem. 47 (2008) 2188–2207. https://doi.org/10.1002/ANIE.200701812.

[38] H.T. Baytekin, A.Z. Patashinski, M. Branicki, B. Baytekin, S. Soh, B.A. Grzybowski, The mosaic of surface charge in contact electrification, Science 333 (2011) 308–312. https://doi.org/10.1126/SCIENCE.1201512/SUPPL_FILE/BAYTEKIN.SOM.PDF.

[39] Y. Wang, Y. Yang, Z.L. Wang, Triboelectric nanogenerators as flexible power sources, npj Flexible Electronics 1 (2017) 1–10. https://doi.org/10.1038/s41528-017-0007-8.

[40] F. Xi, Y. Pang, W. Li, T. Jiang, L. Zhang, T. Guo, G. Liu, C. Zhang, Z.L. Wang, Universal power management strategy for triboelectric nanogenerator, Nano Energy. 37 (2017) 168–176. https://doi.org/10.1016/J.NANOEN.2017.05.027.

[41] J. Chun, B.U. Ye, J.W. Lee, D. Choi, C.Y. Kang, S.W. Kim, Z.L. Wang, J.M. Baik, Boosted output performance of triboelectric nanogenerator via electric double layer effect, Nat. Communications 7 (2016) 1–9. https://doi.org/10.1038/ncomms12985.

[42] S. Niu, Y. Liu, S. Wang, L. Lin, Y.S. Zhou, Y. Hu, Z.L. Wang, Theoretical investigation and structural optimization of single-electrode triboelectric nanogenerators, Adv. Funct. Mater. 24 (2014) 3332-3340. https://doi.org/10.1002/adfm.201303799.

[43] L. Yang, C. Liu, W. Yuan, C. Meng, A. Dutta, X. Chen, L. Guo, G. Niu, H. Cheng, Fully stretchable, porous MXene-graphene foam nanocomposites for energy harvesting and self-powered sensing, Nano Energy. 103 (2022) 107807. https://doi.org/10.1016/J.NANOEN.2022.107807.

[44] J. Yang, P. Liu, X. Wei, W. Luo, J. Yang, H. Jiang, D. Wei, R. Shi, H. Shi, Surface engineering of graphene composite transparent electrodes for high-performance flexible triboelectric nanogenerators and self-powered sensors, ACS Appl. Mater. Interfaces. 9 (2017) 36017–36025. https://pubs.acs.org/doi/10.1021/acsami.7b10373.

[45] M.S. Rasel, P. Maharjan, M. Salauddin, M.T. Rahman, H.O. Cho, J.W. Kim, J.Y. Park, An impedance tunable and highly efficient triboelectric nanogenerator for large-scale, ultra-sensitive pressure sensing applications, Nano Energy. 49 (2018) 603–613. https://doi.org/10.1016/J.NANOEN.2018.04.060.

[46] H.L. Wang, Z.H. Guo, G. Zhu, X. Pu, Z.L. Wang, Boosting the power and lowering the impedance of triboelectric nanogenerators through manipulating the permittivity for wearable energy harvesting, ACS Nano. 15 (2021) 7513–7521. https://pubs.acs.org/doi/10.1021/acsnano.1c00914.

[47] L. Lin, Y. Xie, S. Wang, W. Wu, S. Niu, X. Wen, Z.L. Wang, Triboelectric active sensor array for self-powered static and dynamic pressure detection and tactile imaging, ACS Nano. 7 (2013) 8266–8274. https://pubs.acs.org/doi/10.1021/nn4037514.